On the atmospheric limitations of ground-based submillimetre astronomy using array receivers

E. N. Archibald[1]⋆, T. Jenness[1], W. S. Holland[1,2], I. M. Coulson[1], N. E. Jessop[1],
J. A. Stevens[2,3], E. I. Robson[1,4], R. P. J. Tilanus[1,5], W. D. Duncan[2], and J. F. Lightfoot[2]

[1]*Joint Astronomy Centre, 660 N. Aʻohōkū Place, University Park, Hilo, Hawaii, USA*
[2]*UK Astronomical Technology Centre, Royal Observatory, Blackford Hill, Edinburgh EH9 3HJ, UK*
[3]*Mullard Space Science Laboratory, University College London, Holmbury St. Mary, Dorking, Surrey, RH5 6NT, UK*
[4]*Centre for Astrophysics, University of Central Lancashire, Preston, PR1 2HE, UK*
[5]*Netherlands Organization for Scientific Research (NWO), Postbus 93460, 2509 AL Den Haag, the Netherlands*

ABSTRACT

The calibration of ground-based submillimetre observations has always been a difficult process. We discuss how to overcome the limitations imposed by the submillimetre atmosphere. Novel ways to improve line-of-sight opacity estimates are presented, resulting in tight relations between opacities at different wavelengths. The submillimetre camera SCUBA, mounted on the JCMT, is the first large-scale submillimetre array, and as such is ideal for combating the effects of the atmosphere. For example, we find that the off-source pixels are crucial for removing sky-noise. Benefitting from several years of SCUBA operation, a database of deep SCUBA observations has been constructed to better understand the nature of sky-noise and the effects of the atmosphere on instrument sensitivity. This has revealed several results. Firstly, there is evidence for positive correlations between sky-noise and seeing and sky-noise and sky opacity. Furthermore, 850-μm and 450-μm sky-noise are clearly correlated, suggesting that 450-μm data may be used to correct 850-μm observations for sky-noise. Perhaps most important of all: if off-source bolometers are used for sky-noise removal, there is no correlation between instrument sensitivity and chop throw, for chop throws out to 180 arcsec. Understanding the effects of submillimetre seeing is also important, and we find that the JCMT beam is not significantly broadened by seeing, nor is there an obvious correlation between seeing and pointing excursions.

Key words: submillimetre – instrumentation: detectors (SCUBA) – telescopes (James Clerk Maxwell Telescope)

1 INTRODUCTION

Ground-based observations at submillimetre wavelengths are severely hindered by the atmosphere, which absorbs, emits, and refracts the incoming radiation. High, dry sites are needed, such as Mauna Kea in Hawaii. Even then the transmission is generally poor, with only a small number of semi-transparent windows accessible.

To calibrate submillimetre data, the atmospheric opacity must be accurately determined. The main absorber of radiation in this waveband is water vapour, although oxygen and ozone can be significant contributors. Furthermore, the transparency of the atmosphere often changes on short timescales. Thus, frequent measurements of the opacity are crucial, especially for the shorter wavelength windows at 350 and 450 μm. There is a strong dependence of the transmission on wavelength; the shorter windows are more opaque, and deteriorate faster as conditions worsen.

In addition to attenuating the signal, the atmosphere and immediate surroundings of the telescope emit thermal radiation several orders of magnitude larger than the source signal. Spatial and temporal variations in this sky emissivity give rise to "sky noise", which can degrade the effective instrument sensitivity by up to an order of magnitude. The thermal DC offset and sky noise variability can be largely removed by the conventional techniques of sky-chopping and telescope nodding. To be effective against sky noise requires the secondary mirror to switch between sky+source and sky faster than the rate at which the sky is varying (typically greater than a few Hz). Nodding the telescope primary to place the source alternately in both chop beams cancels slower varying sky gradients due to chop-beam imbalances and time-dependent telescope spillover signals. It is not practical to nod the primary at the chop
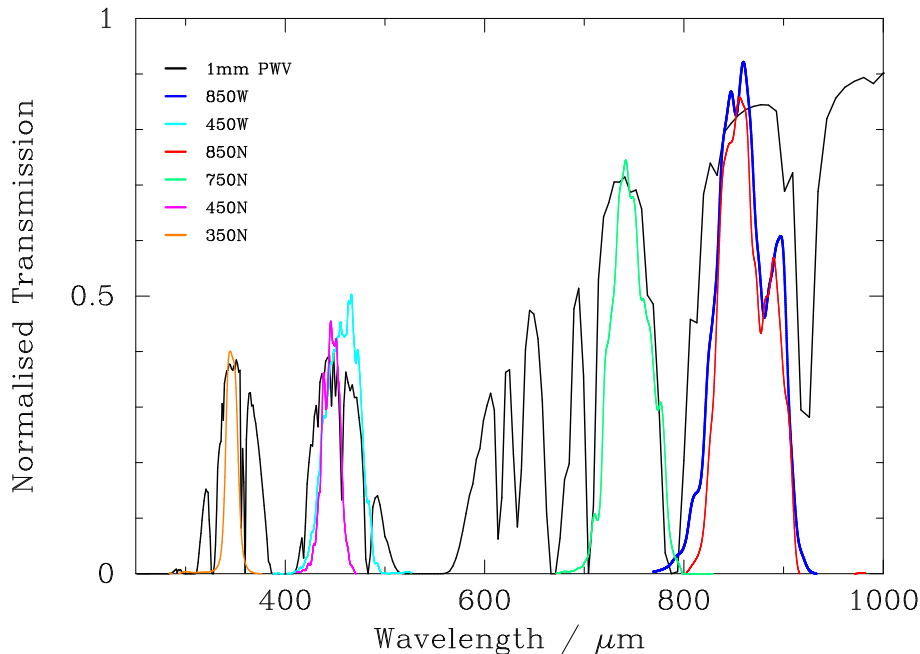
⋆ email: e.archibald@jach.hawaii.edu

Figure 1. The SCUBA filter profiles measured in situ, superimposed on the submillimetre atmospheric transmission curve for Mauna Kea assuming 1 mm of precipitable water vapour.

rate and so typical frequencies of 0.1 Hz are adopted. However, although these techniques diminish the effects of sky noise, they do not remove the residual signature completely.

Fluctuations in the atmospheric refractive index, as the atmosphere drifts through the telescope beam, cause variations in the path length from source to telescope (Church & Hills 1990; Church et al. 1993). This is sometimes referred to as submillimetre seeing, and causes apparent (short-term) pointing shifts, which ultimately degrade the S/N of an observation. This is particularly problematic for under-sampled arrays such as SCUBA. Until the time that adaptive optics becomes available for the submillimetre, the effects of this seeing must be closely monitored, and the data severely affected removed from a particular observation.

This paper considers the limitations imposed on the quality of submillimetre data by the atmosphere, and presents methods that maximise the accuracy of the data. The layout is as follows: Section 2 provides a technical description of SCUBA and its advantages compared with previous instruments, while Section 3 discusses techniques of determining atmospheric extinction as a function of wavelength. We present our own skydip model and consider how continuously-operating radiometers are crucial for precise measurements of atmospheric opacity. Sky-noise is described in detail in Section 4, particularly how it can degrade instrument sensitivity, and how most of its effects can be removed with state-of-the-art instrumentation such as SCUBA. The effects of refraction noise (submillimetre seeing) are described in Section 5. Using a carefully constructed database of SCUBA observations and atmospheric information, Section 6 analyses how the atmosphere directly effects instrument sensitivity. In Section 7 we conclude with a discussion of future technology that will provide further improvements in the accuracy of submillimetre data.

2   THE BENEFITS OF ARRAY RECEIVERS: SCUBA

Until recently, observing in the submillimetre was limited to single-pixel devices. UKT14 (Duncan et al. 1990), the forerunner to SCUBA on the JCMT, was detector-noise limited at all wavelengths of operation, except under periods of high sky variability, when the sensitivity at 350 and 450 µm was severely limited by sky-noise.

An array receiver is a major improvement over a single-pixel system. The off-source pixels can be used to measure sky-noise on short timescales. This is crucial for accurate work: Omont et al. (1996) compared the performance of a detector array with a single-pixel system, and found that the poor sky cancellation offered by a single detector could in fact produce fake detections of faint sources.

Within the past few years submillimetre astronomy has witnessed the arrival of the first large format bolometer arrays, together with detector sensitivities which are limited, under stable conditions, by the background photon noise from the sky. The largest and most powerful of this new generation of submm cameras is the Submillimetre Common-User Bolometer Array (Holland et al. 1999), which operates on the 15-m James Clerk Maxwell Telescope, on Mauna Kea. SCUBA is a dual camera system containing 91 pixels in the short-wavelength (SW) array and 37 pixels in the long-wavelength (LW) array. Background-limited performance is achieved by cooling the detectors to ~ 100 mK. Both arrays have approximately the same field-of-view (FOV) on the sky (2.3 arcminutes in diameter) and can be used simultaneously by means of a dichroic beamsplitter. The SW array is optimised for operation at 450 µm, while the LW array is optimised for 850 µm.

The wavelength of operation is selected by a bandpass filter carefully designed to match the transmission window. The filters are multi-layer, metal-mesh interference filters (Hazell 1991) located in a nine-position rotating drum that surrounds the arrays. They have excellent transmission (typically over 80%), and also less than 0.1% out-of-band power leakage. This latter characteristic is particularly important as it ensures that there is minimum con-

tribution to the source signal from extraneous sky emission. The spectral performance of the filters was measured by the University of Lethbridge Fourier Transform Spectrometer (Naylor et al. 1994), and the resultant profiles are overlaid on the Mauna Kea atmospheric transmission curve in Figure 1. For a more detailed look at the submillimetre atmosphere please refer to Naylor et al. (2000).

SCUBA has three basic observing modes (Holland et al. 1999). Photometry, uses a single bolometer to observe point sources. For sources larger than the beam, but smaller than the array FOV, a 64-point jiggle map produces a fully-sampled map for both the LW and the SW arrays, by jiggling the secondary mirror to fill in the undersampled arrays. Finally, sources larger than the array FOV are observed in scan-map mode.

The SCUBA Upgrade Project was designed to improve the sensitivity of the instrument. The first part of the project was completed in October 1999, and included the installation of two wideband filters centred at $450\,\mu$m and $850\,\mu$m (450W:850W). The wideband filters were designed to be more closely matched to the atmospheric windows (Figure 1), and to be more sensitive than their narrowband predecessors (450N:850N) under all weather conditions. The measured improvement is a few percent at $850\,\mu$m and a factor of 2 at $450\,\mu$m. The improvement at $850\,\mu$m is not due to the width of the filter, but to the blocking filter that was installed to reduce contamination by infrared light. The overall spectral transmission characteristics of the 850-μm waveband are driven by the edge filters and detector feed-horn cut-off. Thus, unfortunately, the measured response of the 850-μm wideband filter is almost identical to that measured for the narrowband filter. For the purposes of this paper, we will concentrate on the 450W:850W filters.

3 ATMOSPHERIC ATTENUATION

Determining the atmospheric attenuation of a source signal is critical for calibrating submillimetre data. Assuming a plane-parallel atmosphere:

$$I_m = I_\circ e^{-TauA} \tag{1}$$

where I_m and $I_\circ$ are the signals incident at the telescope and at the top of the atmosphere respectively, A is the airmass (the secant of the zenith distance), and Tau is the zenith sky opacity (Stevens & Robson 1994). Thus, precise measurements of Tau must be taken frequently. This is less crucial at $850\,\mu$m; in good weather, $Tau_{850} < 0.3$, and at low airmass, (<1.5), a 20% error in Tau_{850} alters the measured source flux density by 5-10% at most. However, in worse conditions and particularly at $450\,\mu$m, an error in Tau can severely affect the measured source flux density. For example, assuming a low airmass <1.5, a 20% error in Tau_{450} can alter the measured flux density by $\sim 50 - 80\%$.

Traditionally, Tau was derived by constructing a secant plot: the signal from the source is measured as a function of airmass, and assuming the sky does not change between measurements, the gradient of the plot gives Tau directly. However, this method requires a meaningful number of measurements of a bright source over a range of airmasses. For any level of accuracy, the sky must remain very stable over a long period of time. Stevens & Robson (1994) demonstrate the difficulties of using this method to derive Tau. We describe here alternative methods that are able to track rapid variations in Tau.

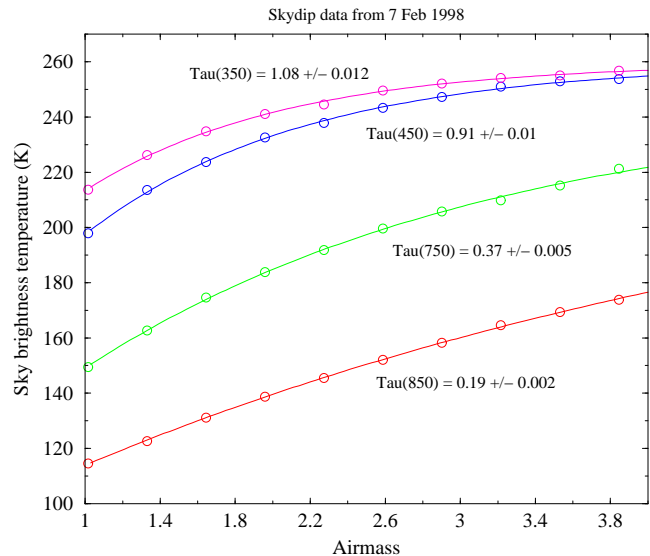SCUBA skydips at 350, 450, 750 and 850 microns

Figure 2. Typical skydip examples at 350, 450, 750 and 850 μm. Open circles denote measurements taken with SCUBA; solid lines denote the model fits to the data. The skydips shown here correspond to a precipitable water vapour of ~ 0.7mm (see Equation 3).

3.1 Skydip method

SCUBA estimates the zenith sky opacity at the wavelength and azimuth of observation by performing skydips. Skydips measure the sky brightness temperature as a function of elevation (usually between 80 and 15 degrees), with absolute temperature calibration provided by hot and cold loads. The hot load is ambient temperature Eccosorb, and the cold load is a reflection of the cold optics inside the cryostat, with an effective temperature of ~ 60 K. An aperture plane chopper unit, spinning at 2 Hz, is used to switch rapidly between the sky and the two loads. The temperatures of the hot and cold loads are measured and corrected for the emissivity and reflectivity of the components in the optical path. A model describing both the atmosphere (assuming a plane-parallel form) and the optical system is then fit to the data to calculate the zenith sky opacity:

$$J_{meas} = (1 - \eta_{tel})\,J_{tel} + \eta_{tel}\,J_{atm} - bwf\,\eta_{tel}\,J_{atm}e^{-TauA} \tag{2}$$

where J_{meas} is the measured brightness temperature of the sky, η_{tel} is the transmission of the telescope, J_{tel} is the brightness temperature of a black-body radiating at the temperature of the telescope, J_{atm} is the brightness temperature of the atmosphere, bwf is the bandwidth factor of the filter being used ($1 - bwf$ is the fraction of the filter bandwidth that is opaque due to atmospheric absorption and, like Tau, is a function of water vapour content), Tau is the zenith sky optical depth and A is the airmass of the measurement. Technical details of this model are presented in Appendix A, refer also to Hazell (1991).

Figure 2 shows typical skydips taken with SCUBA at several wavelengths. In practice, the skydip method provides an accurate measurement of Tau. However, it takes ~ 6 minutes to perform a skydip. Given this overhead, it is only practical to perform a skydip every 1.5-2 hours, and quite often the frequency is even less. An on-the-fly skydip mode has recently been commissioned, where data are taken continuously, reducing the time taken to $\sim 2 - 3$ minutes (Coulson 2001).
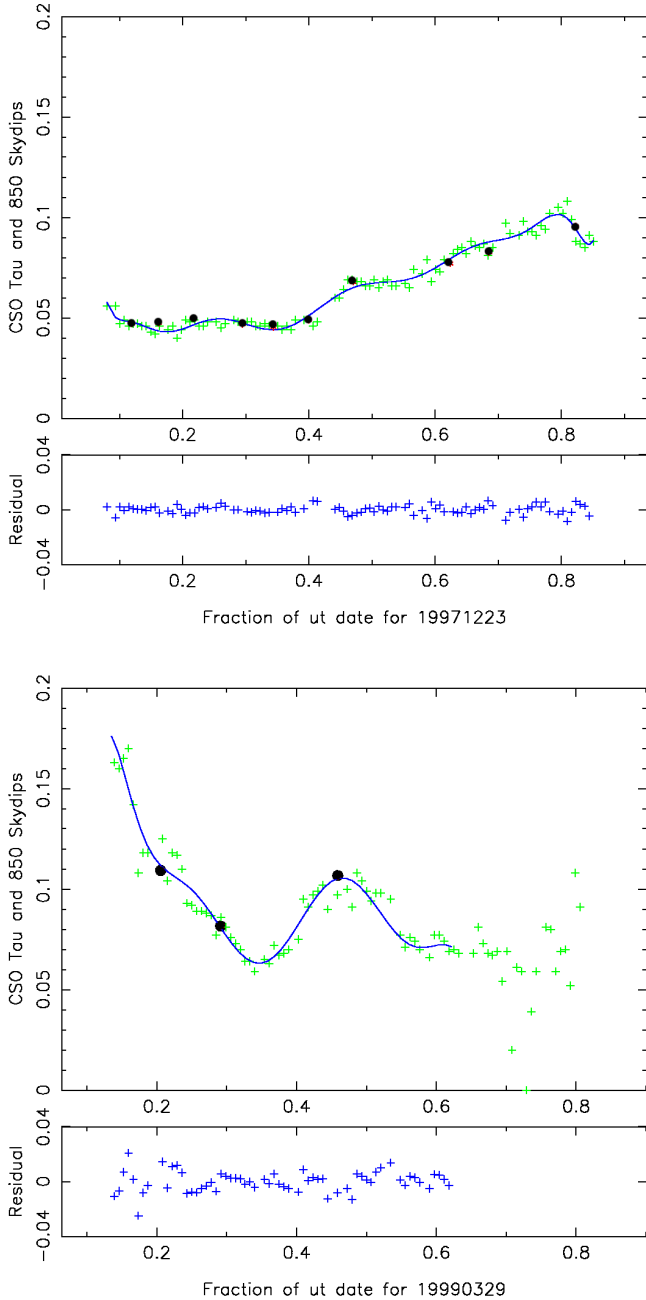
Figure 3. CSO Tau data as a function of time (expressed as a fraction of the UT date) for two typical nights. The CSO data are depicted by the '+' symbols. The 850-micron skydips taken for each night, scaled to 225 GHz values using the newly derived CSO Tau relations(Section 3.3), are denoted by the solid circles. The solid line is a polynomial fit to the CSO Tau data. The fit residuals are also shown.

3.2 CSO Tau Monitor

The nearby Caltech Submillimetre Observatory (CSO) operates a 225 GHz (1.25 mm) tipping radiometer, which performs a skydip every 10 minutes, albeit at a fixed azimuth. The precipitable water vapour of the atmosphere is related to the CSO Tau as follows :

$$pwv = 20(Tau_{CSO} - 0.016) \qquad (3)$$

where the pwv is in millimetres (Davis et al. 1997).

Comparing skydips taken with SCUBA to those taken at the CSO yields relations between Tau_{CSO} & Tau_{850} and Tau_{CSO} & Tau_{450}. If the scatter about these relations is small, the CSO Tau monitor can be used to measure the opacity more frequently than we can with SCUBA, with no additional overhead.

The CSO data show a significant amount of noise, but track long time-scale ($\sim$2 hour) variations very well. This noise is more than one would expect given the measurement errors quoted in the CSO Tau archive. It is probable that this is due to instrumental noise and does not represent the behaviour of the sky. A polynomial can be fit to the data to track the large-scale variations in CSO Tau as opposed to the (presumably) instrument noise.

In Figure 3, example polynomial fits are presented for two typical nights. Using the relations derived in Section 3.3, we have also plotted the 225 GHz Tau predicted by the 850-μm skydips taken each night. It is striking how well the skydips track the polynomial fits, even when one would imagine that the CSO Tau was moving around too much to be useful.

Producing a composite picture of the night, using the CSO Tau, the SCUBA skydips, and the polynomial fit, provides an additional level of quality control. It can give the observer a much better feel for how the atmosphere was actually behaving on a given night, especially if conditions were apparently unstable. Consider first the lower plot in Figure 3. It is clear that interpolating between the SCUBA skydips would give an erroneous measurement of Tau. In addition, the extreme scatter in CSO Tau indicates that the end of the night was unusable.

The composite picture can provide further information about when data should be treated with care. For example, on some nights the CSO Tau and SCUBA skydip data disagree with each other, on other nights both display unusually high levels of scatter, indicating an inherently unstable night. If, on the other hand, the CSO Tau has a high-level of scatter but the SCUBA skydips follow the polynomial fit, the scatter is unlikely to be representative of the sky itself.

3.3 Tau relations

The time-resolution of the polynomial fits to the CSO Tau is impressive, $\sim$ 2 minutes if the residuals are small, as they typically are. We can capitalise on this by deriving tight relations between the CSO Tau and the opacity measured at SCUBA wavelengths.

These relations have been constructed taking the following points into account:

(i) Skydips were discarded where the model failed owing to, for example, the atmosphere losing its plane-parallel nature or a cloud drifting overhead. In these cases the model returns unrealistic values for the fit parameters and/or unusually high fit residuals. This is a more common occurrence at 450 μm, where the shape and height of the atmospheric window are more sensitive to the presence of water vapour (see Figure 1). We discarded $\sim$20% of the data at 850 μm and $\sim$50% of the data at 450 μm. Note, we can still calibrate at 450 μm when the skydip fit fails as we can extrapolate from either the CSO or the 850-μm Tau.

(ii) We ignored data taken when the CSO Tau monitor was offline.

(iii) If either the CSO Tau monitor or the skydip indicated a nonphysical value of Tau, i.e. negative or zero, the observation was ignored.
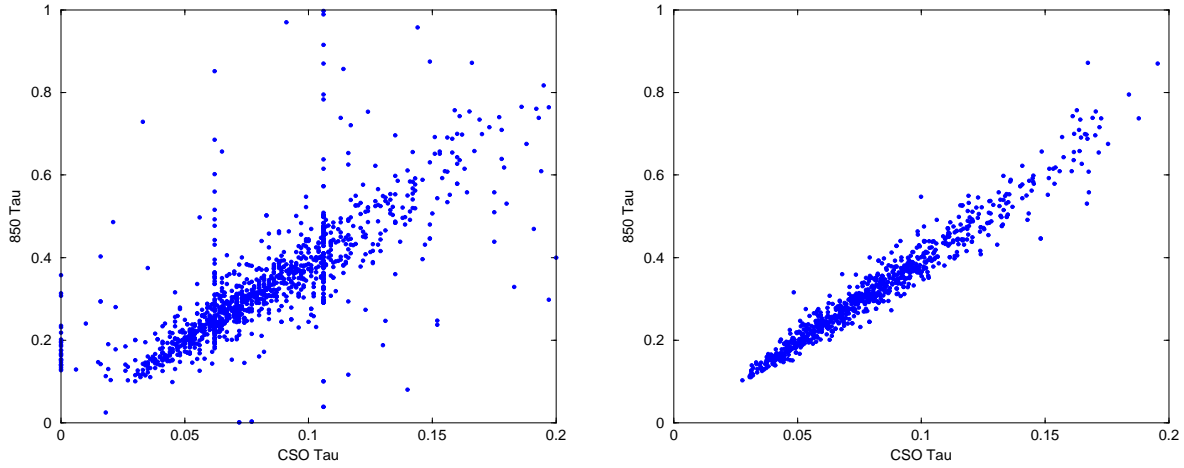
Figure 4. The wideband Tau_{850}-Tau_{CSO} relation. For the left plot, the CSO Tau data were taken directly from the archive, and every skydip observation was accepted. The right plot shows the relation with Tau_{CSO} calculated from the polynomial fits, and with the poor-fitting skydips having been removed.

Filter System	Time Period	Tau_Y	Tau_X	$Tau_Y = a(Tau_X - b)$	
				a	b
450N:850N	Feb. 04, 1998-Oct. 10, 1999 (pre-upgrade)	Tau_{850}	Tau_{CSO}	3.99$\pm$0.02	0.004$\pm$0.001
		Tau_{450}	Tau_{CSO}	23.5$\pm$0.2	0.012$\pm$0.001
		Tau_{450}	Tau_{850}	5.92$\pm$0.04	0.032$\pm$0.002
450W:850W	Dec. 05, 1999-Sept. 30, 2000 (post-upgrade)	Tau_{850}	Tau_{CSO}	4.02$\pm$0.03	0.001$\pm$0.001
		Tau_{450}	Tau_{CSO}	26.2$\pm$0.3	0.014$\pm$0.001
		Tau_{450}	Tau_{850}	6.52$\pm$0.08	0.049$\pm$0.004

Table 1. Tau relations for both the narrow and wide 450:850 filter systems, calculated using least-squares regression. The corresponding errors are $1 - \sigma$. The relations have been constructed using the CSO polynomial fits and by ignoring poor-fitting skydips.

(iv) The datasets were restricted to $Tau_{CSO} < 0.2$ (SCUBA is not used in weather conditions worse than this).

(v) A model of the form $Tau_Y = a(Tau_X - b)$ was fit to the data to derive the Tau relations.

Figure 4 shows how much the scatter in the relations has been reduced by simply using the polynomial fits to estimate the CSO Tau and ignoring untrustworthy skydips. The final relations are presented in Table 1 and Figure 5. They display relatively little scatter, even in the poorest weather conditions, and can thus provide accurate submillimetre calibration.

Comparing the wideband and narrowband filters, the wideband CSO Tau relations are steeper at 450 μm but are almost identical at 850 μm. At first sight, the difference at 450 μm is perhaps unexpected given the lower central wavelength of the wideband filter (at 850 μm, the narrow and wideband filters have almost identical central wavelengths). However, the 450 μm wideband filter includes an H_2O line that is always present, even in very dry weather conditions. Thus, the wideband filter will always have a steeper slope than the narrowband filter.

If the submillimetre opacity is due solely to water vapour, the Tau relations for the different filters are expected to intercept the origin: if there is no water vapour in the atmosphere, Tau_{CSO}, Tau_{850} and Tau_{450} will all equal zero. However, we have found evidence for non-zero intercepts. Assuming the straight-line model can be extrapolated to the intercept, this could be explained as follows: the relative contribution of ozone vs. water vapour to absorption is greater at 225 GHz than at 850 μm and in turn greater at

850 μm than at 450 μm. The ozone contribution is relatively invariant for long periods of time, and these offsets should be constant.

4 SKY-NOISE

4.1 Signatures of sky-noise

The atmosphere emits submillimetre radiation several orders of magnitude larger than the signals we are trying to measure. Variations in this emission result in sky-noise, which manifests itself as a 1/f component in the noise spectrum. This is illustrated in Figure 6, where the 1/f component extends out to 4 Hz and is well above the system noise level. Two-position chopping at higher frequencies, ~ 8 Hz, greatly reduces this sky-noise contamination (Duncan et al. 1995).

As noted earlier, telescope nodding is also essential for the removal of sky-noise. This can be illustrated by the Allan variance, which is simply the variance of the difference of two contiguous measurements (e.g., Allan 1966; Schieder & Kramer 2001). When plotted, a slope of -1 indicates white noise, a slope of 0 denotes 1/f noise, and a slope of $+1$ is drift noise. Figure 7 shows the Allan variance data as a function of time for a typical observation with and without nodding (in both cases the telescope was chopping at ~ 8 Hz). A clear 1/f component is present if the telescope is not nodded: after around 20 seconds the noise stops integrating down. This component disappears when nodding is employed.

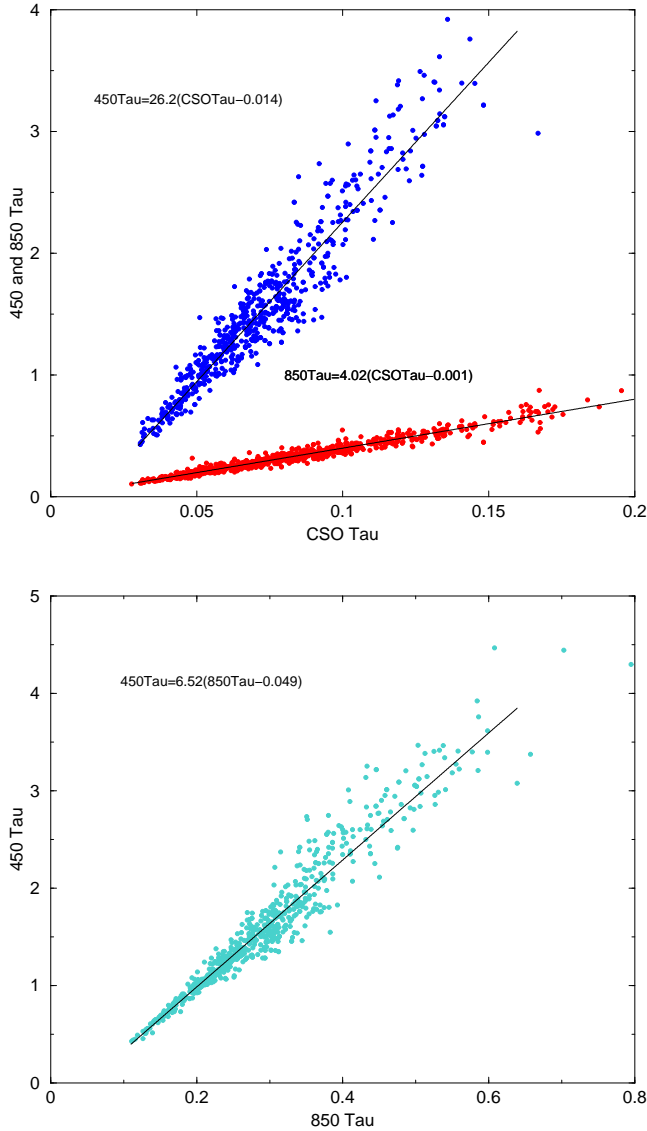However, it is impractical to nod the telescope at the chop

Figure 6. Noise spectrum for LWA central pixel, showing 1/f noise tail of sky-noise. The system noise trace is from the central bolometer looking at a 4 K blank placed over the arrays.

Figure 7. Allan variance plot showing 1/f noise, white-noise and drift noise.

Figure 5. Tau relations for the wideband 450W:850W filter system. The top plot depicts the relationship between the SCUBA skydips and CSO Tau. The bottom plot depicts the Tau_{450}-Tau_{850} correlation derived by comparing 450-µm and 850-µm skydips. Models of the form $Tau_Y = a(Tau_X - b)$ have been fit to the data in every case.

4.2 Removal of sky-noise

In the submillimetre, the emissivity variations occur in atmospheric cells that are larger than the array field-of-view (Jenness et al. 1998; Borys et al. 1999). Therefore, the noise should be correlated to a large extent across the array and also between wavelengths.

One of the main advantages of SCUBA is that it contains an array of bolometers. When observing a compact source, the off-source bolometers can be used to measure the sky signal on short timescales and hence remove any residual sky-noise that chopping and nodding have failed to account for.

This is clearly illustrated in Figure 8, where the signal of both the centre on-source 850-µm pixel and the sky (measured by averaging the outer ring of bolometers) are shown. The signals are highly correlated, and subtracting the sky from the source reveals a clear positive signal (in which the jiggle modulation is apparent). Using this sky-subtraction method can improve the S/N significantly. In Figure 8 we also display the 450-µm centre pixel, and, as expected, it is also highly correlated with the 850-µm data.

frequency. Thus, even with a chop/nod configuration, short-term temporal variations in the sky emissivity, as well as spatial effects caused by chopping through slightly different atmospheric paths, still exist. This residual sky-noise must be removed. There are several ways to do this; filters can be designed to select the most transparent parts of the atmospheric transmission window. The optical throughput should be single-moded, i.e. the minimum required to couple to a point source with maximum spatial resolution and minimum background (Duncan et al. 1995). Keeping the chop throw as small as possible, and in an azimuthal direction (i.e. chopping through the same atmospheric layer), should also help. In this paper we will concentrate on the benefits of having a bolometer array to aid the removal of sky-noise.
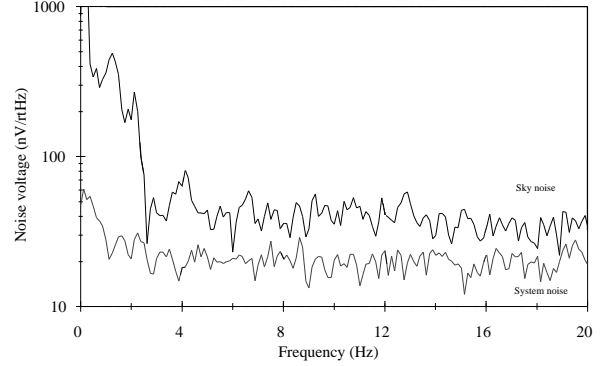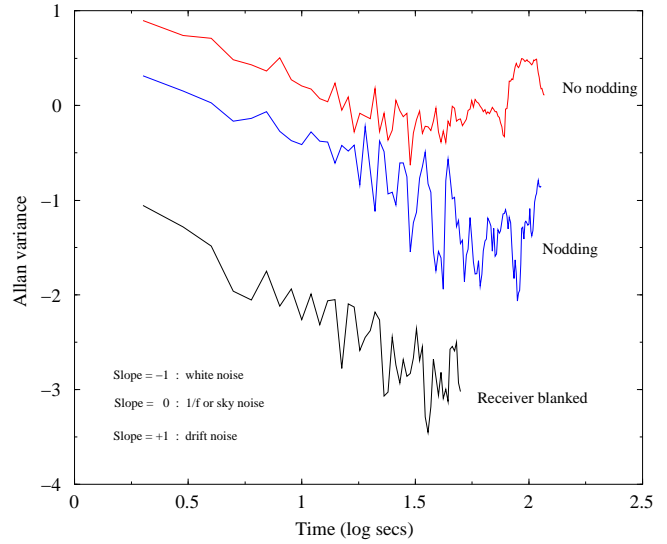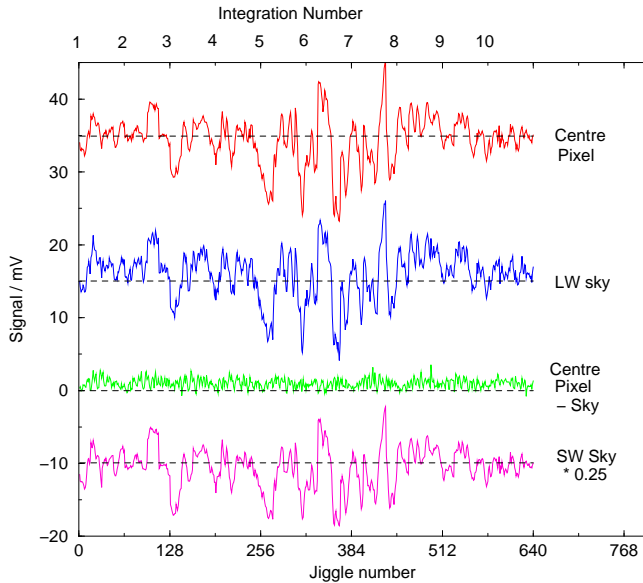
Figure 8. Example of the identification and removal of sky-noise. This figure first appeared in Holland et al. (1999) - note one integration comprises 128 seconds, split into 4 exposures of 16 jiggle points, with 1 second observed per jiggle point per nod position (there are two nod positions).

Figure 9. Standard error evolution with time for a deep 850-µm photometry observation. For the open circles, only chopping and nodding have been used for sky cancellation. For the solid circles, the sky-noise residual has been removed using the off-source bolometers. This data was, for the most part, taken in uncommonly stable weather conditions.

Failure to remove this residual sky-noise can, in the worst conditions, degrade the sensitivity of the instrument by an order of magnitude. Figure 9 displays the noise integrating down with time for a deep 850-µm photometry observation. Data are shown for the standard chop/nod configuration, and also after the residual sky-noise has been removed using the off-source bolometers. We define the sensitivity, also known as the noise equivalent flux density (NEFD), as the noise reached in 1 sec of integration. It is clear that the NEFD of the instrument is significantly better if the residual sky-noise is removed. Furthermore, at the end of the observation, there was a very obvious, large deterioration in the sky conditions. This is plainly visible in the case where the residual sky-noise was not removed. Removing the residual takes this change of conditions into account, and allows the noise to integrate down $\propto \sqrt{t}$.

For scan-map observations, removing the sky-noise is more difficult, as every bolometer could be observing either the source or the sky at a given time. The source can be removed from the datastream by the simple assumption that the source structure is constant over time, while the sky is varying on timescales of a few seconds. The sky-emission noise can then be calculated and removed from the data (Jessop et al. in preparation).

4.3 Investigation of sky-noise

For the purposes of this paper, we define sky-noise as the standard deviation of the sky signal, with any errors associated with nodding removed. The dataset used here consists of deep photometry observations only, as it is easy to specify the sky bolometers and the long observations provide good statistics.

The relationship between sky-noise, seeing, and sky opacity is not immediately obvious; the scatter in the data was too large to reveal an obvious trend. To overcome this, we binned the data. This also posed problems as the data were not Gaussian distributed and it was not clear whether the mean (which is skewed by outliers) and associated standard deviation (which is unnaturally large given the scatter in the data) were useful quantities to measure. Instead
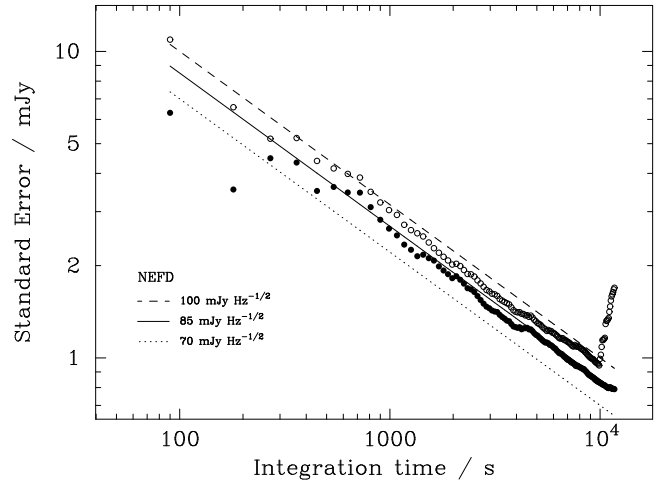
we measured the mode and full-width half-maximum of the data in each bin. These plots are shown in Figure 10, and although the 'errors' are somewhat large, there is evidence for positive correlations between sky-noise and seeing and between sky-noise and Tau. There is, however, no evidence to support the long-standing belief (from single-pixel instruments) that sky-noise often increases in very dry weather conditions.

Considering the 850-µm and 450-µm sky signals for 20 minute photometry observations, Figure 11 presents a histogram of the Spearman-rank correlation coefficients. A value of +1 indicates a pure positive correlation, 0 indicates no correlation, and -1 indicates a pure negative correlation. On the whole, the 850-µm and 450-µm data appear to be highly correlated. However, there are clearly times when the strength of the correlation is low.

Given the known correlation between sky-noise at 850 µm and 450 µm, it has been suggested that the short wavelength array could be used to provide sky cancellation at 850 µm. This would be extremely useful for faint sources where the 450 µm field-of-view is likely to be source-free, but the 850 µm field is expected to contain several sources or extended structure.

The ratio of the 450-µm sky signal to the 850-µm sky signal (corrected for extinction) is displayed in Figure 12. For the narrowband data, the median ratio is ~ 4.5 in agreement with Borys et al. (1999) and Jenness et al. (1998); for wideband data, the median ratio is ~ 8 and the distribution is wider. The ratio shows less dispersion if it is extinction corrected than if not, suggesting that the water vapour creating the sky-noise is higher up in the atmosphere rather than just above the telescope (where zero correction would be more suitable).

In Figure 13 we present the ratio of 450-µm:850-µm sky-noise as a function of the corresponding transmission ratio. Thus, for a given transmission ratio, it is possible to use this plot to correct 850-µm data for sky-noise using 450-µm sky-noise data. It is clear that the sky-noise is larger for the wideband filter set than for the narrowband. This difference is to be expected as the 450-µm wideband filter is double the bandwidth of its narrowband predecessor, and contains an H_2O absorption line, while the two 850-µm filters have almost identical bandwidths (Duncan 1983 showed analytically that for a sky-limited system $NEP \propto \Delta\nu$). This ex-
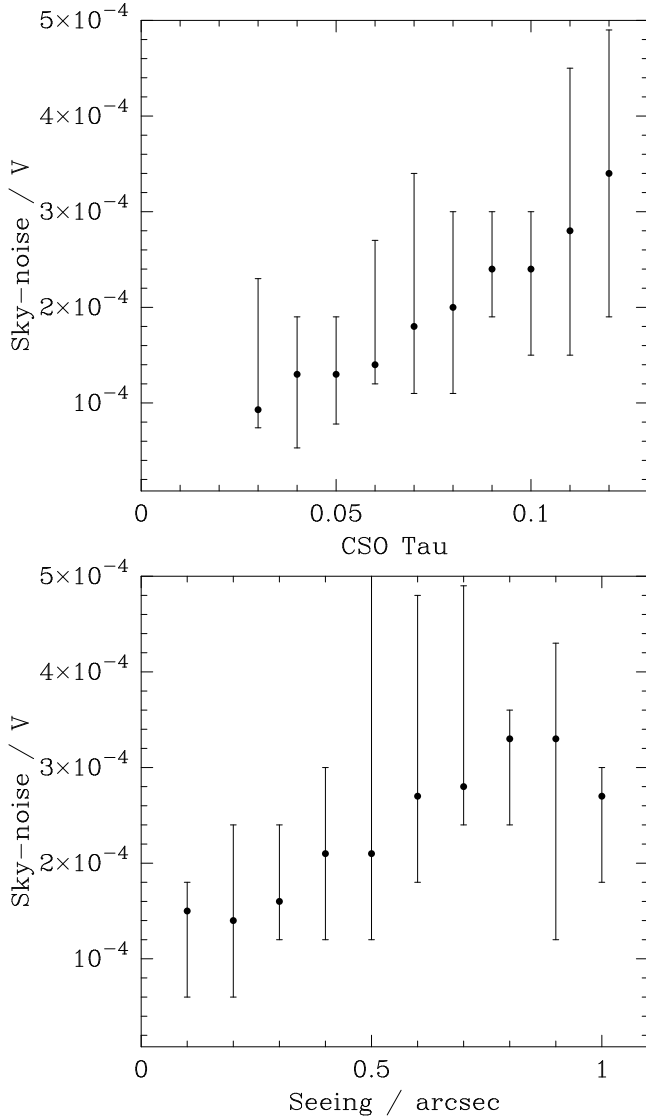
Figure 10. 850-µm sky-noise binned in CSO Tau (top plot) and seeing (bottom plot). The data points are the mode of each bin, and the 'errors' are the corresponding full-width half-maxima.
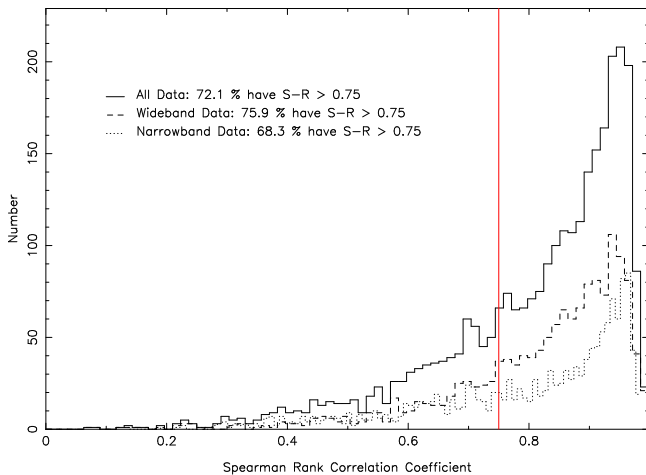

Figure 11. Histogram of Spearman-rank correlation coefficients comparing 850 µm and 450 µm sky signals.
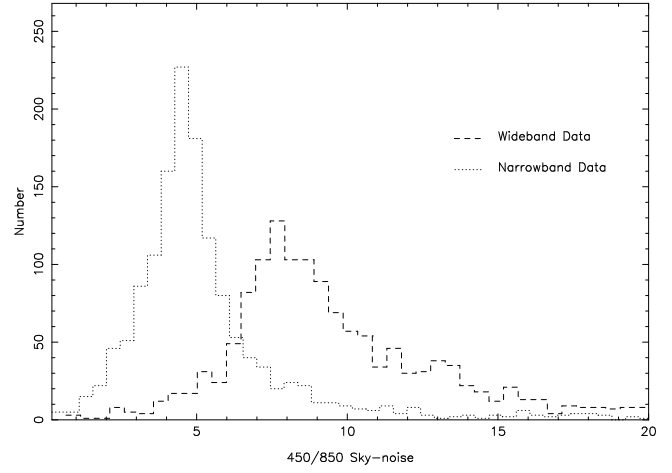

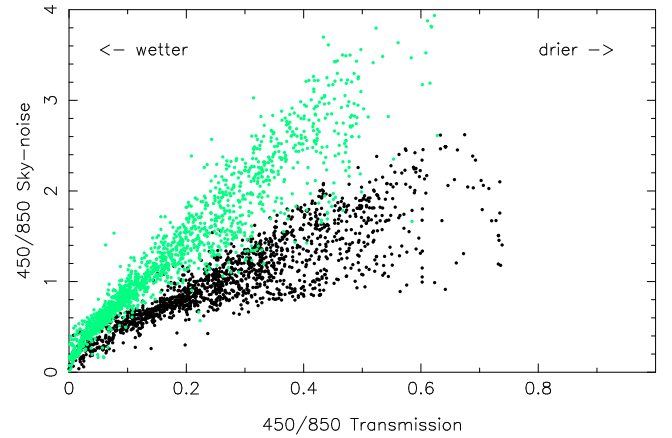**Figure 12.** Histogram of the ratio of 450-µm sky signal to 850-µm sky signal.

Figure 13. The 450-µm:850-µm sky-noise (not corrected for extinction) ratio against the 450-µm:850-µm transmission ratio. The black circles denote the narrowband filter, the gray circles denote the wideband filter.

cess sky-noise is the cost of the improvement in sensitivity offered by increasing the 450-µm bandwidth. However, as we have already demonstrated, this excess is removable with a bolometer array.

A transmission ratio of 1 in Figure 13 corresponds to there being no atmosphere between the telescope and the source of the sky-noise. If the sky-noise ratios in Figure 13 are extrapolated to a transmission ratio of 1, we find values of ~ 3.5 and ~ 6.5 for the narrowband and wideband filters correspondingly. These numbers are in good agreement with the theoretical values derived in Appendix B. The extinction-corrected ratios in Figure 12 are larger however, indicating that we are over-correcting for extinction in calculating these ratios. This in turn suggests that the water vapour responsible for the sky-noise lies somewhere in the middle-upper layers of the atmosphere, not at the very top of the atmosphere itself.

5   SUBMILLIMETRE SEEING

5.1   Measurement on Mauna Kea

Submillimetre seeing arises from variations in the refractive index of the atmosphere, principally due to the passage of water vapour
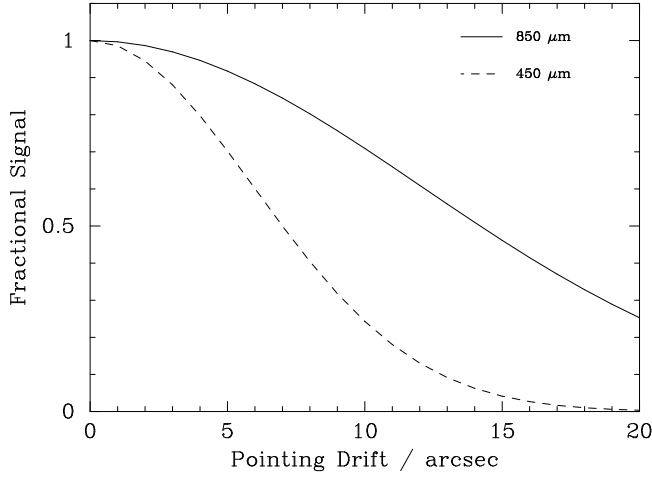
Figure 14. Fractional signal as a function of pointing drift, assuming a FWHM of $14.2''$ at 850 μm and $7''$ at 450 μm.

through the beam. This variation is measured on Mauna Kea by a phase monitor operated by the Smithsonian Astrophysical Observatory (SAO). The SAO device comprises two 1.8 m dishes placed about 100 m apart located near the JCMT. The dishes point low in the eastern sky, and detect a signal at 12 GHz from a geostationary satellite. The difference in path lengths results in a phase difference between the two received signals that changes slowly with the oscillation of the satellite position. Turbulence in the atmosphere adds noise to the phase difference. The phase difference is measured each second and one minute's worth of data are analysed for the rms scatter to provide the seeing at 12 GHz over a 100 m baseline.

The conversion from the rms of these phase fluctuations to an rms seeing for the 15 m JCMT is suggested by Masson (1991) as being:

JCMT seeing (arcsec rms) = 0.5 SAO seeing (degrees rms)

Fifteen minute averages of these seeing data are available at the JCMT as part of the Telescope Management System (Tilanus et al. 1997). By the middle of the night the JCMT seeing typically drops to 0.2 arcsec, and observers consider seeing > 1 arcsec to be 'poor'.

5.2 Impact of seeing: broadening & displacement

If atmospheric turbulence on scales smaller than the telescope diameter is significant then beam-broadening will occur. However, experiments by Church & Hills (1990) indicate that these effects are small at the JCMT. Beam displacement results from large-scale, anomalous refraction, or 'tip/tilt' effects, and effective beam-broadening results if observations take longer than the timescale of these fluctuations; the time average of the beam motion being superimposed on the beam profile. Anomalous refraction timescales are of order 1 s (Olmi 2001), which is considerably shorter than standard JCMT observations (minimum 18 s), but comparable with the SAO monitor rate. JCMT jiggle maps (integration times > 32 s) therefore suffer both minimal average pointing shifts and minimal image broadening as the turblence tends to occur on scales larger than the telescope diameter.

Additionally, analysis of JCMT tracking data shows that there is no correlation between seeing and pointing excursions. Tracking data are long jiggle maps of bright point sources, and each integration (32 s worth) is analysed for the location of the image centroid

to yield information on pointing offsets as a function of azimuth, for instance. Some tracking datasets cover a sufficiently long time interval that significant changes in seeing occur. Within such data there is no correlation between the change in seeing and excursions in pointing.

Tracking data also tend to validate the conversion factor (0.5) between the SAO phase (rms, degrees) and JCMT-seeing (rms, arcseconds), since the scatter of the pointing offsets about some low-order polynomial fit is usually of the same size as the JCMT-seeing.

5.3 Do errors in computed refraction generate pointing errors?

Relatively thin atmospheric layers (thicknesses < 100 m, say) with arbitrary values of temperature, pressure, and humidity have no impact upon the overall refraction: the refraction towards the normal of a ray entering such a layer is nullified by the refraction away from the normal upon exit. Image displacement (a change in pointing) must therefore result from either non-linear atmospheric structures or from uncompensated changes in local humidity.

The latter hypothesis is simple enough to test using archived JCMT/SCUBA pointing data, and no such relationship is found. The formulae in Appendix C1 show that, to first order and at constant zenith distance, elevation pointing corrections of $0.0768(h - 20)$ arcseconds need to be applied to account for the impact of local humidity, $h(\%)$. In the absence of this correction a plot of the change in elevation pointing against the change in humidity would be expected to have a slope of 0.0768, whereas a plot of the same data perfectly corrected for humidity will have a slope of zero. Analysis of 3000 pairs of consecutive pointing measures yields a slope of -0.009 ± 0.018, commensurate with the latter scenario. The source of residual pointing shifts therefore would seem to be excursions from the idealized atmospheric model - i.e. turbulence - which is probably no great surprise.

5.4 Impact of pointing errors upon flux measurements

Whatever their origin, pointing errors of size θ (arcseconds) cause a signal of strength S_o to be measured as

$$S = S_o \, exp\left[-4 \, ln(2) \, \left(\frac{\theta}{FWHM}\right)^2\right] \qquad (4)$$

where FWHM is the full width at half-maximum of the Gaussian beam. These are shown graphically in Figure 14 in the cases of the JCMT operating at 850 μm and 450 μm.

As to the distribution of pointing errors as a result of refraction noise, we have determined that the expected signal, $< S >$, is related to the true peak signal, S_o, by

$$S_o / < S > \; = \; 1 \, + \, 0.0275 \, \sigma^2 \text{ for a } 14.2'' \text{ beam at 850 μm}$$

$$S_o / < S > \; = \; 1 \, + \, 0.1132 \, \sigma^2 \text{ for a } 7'' \text{ beam at 450 μm}$$

where σ is the rms refraction noise. The full derivation of these equations can be found in Appendix C2.

6 THE EFFECT OF THE ATMOSPHERE ON SENSITIVITY

We have recently made a concerted effort to characterise SCUBA's performance. One aspect of this work was the creation of a database of calibration observations. The key result from studying this data
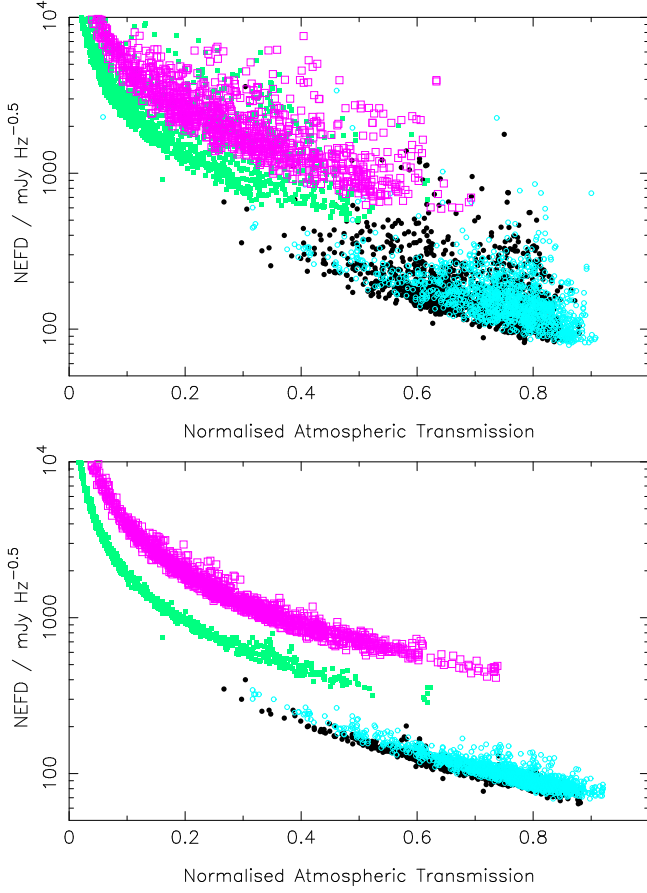
Figure 15. SCUBA sensitivity as a function of normalised sky transmission for the 850W (black circles), 850N (open blue circles), 450W (green squares), and 450N (open pink squares) filters. For the top plot, only chopping and nodding were used for sky cancellation. For the bottom plot, the off-source bolometers were also used for sky cancellation.

Figure 16. NEFD vs. chop throw for both the wide and narrowband 850-μm filters. The dataset is restricted to the normalised sky transmission lying between 0.5 and 0.75, and the values are normalised to a transmission value of 0.65. The top plot is for a chop/nod method of sky cancellation and is restricted to observations with an azimuthal chop throw. In the bottom plot off-source bolometers are used to remove the residual sky-noise, and there is no restriction on the chop throw angle.

is that the flux conversion factors (FCFs) are quite stable, to an accuracy of 5% at 850 μm and 20% at 450 μm (Jenness et al. 2001). Using this database, we have created a homogeneous dataset of $\sim$ 4000 calibrated photometry observations, to better understand the effect of the atmosphere on sensitivity.

Figure 15 presents the NEFD as a function of normalised sky transmission for a chop/nod configuration, and also using the off-source bolometers to remove the residual sky-noise. The NEFD is significantly lower and is inherently more stable if the off-source bolometers are used for sky-cancellation. Data are shown both for the wideband filters, and the pre-upgrade narrowband filters. It is worth noting that the 450-μm wideband filter (which is better matched to the entire atmospheric window but includes an H_2O line) is considerably more sensitive under all conditions. There is little difference between the narrow and wideband 850-μm filters, which is to be expected because, as noted in Section 2, the overall filter transmission profiles are almost identical as measured in SCUBA.

We have also considered how the sensitivity of the instrument is affected by the chop throw. Figure 16 presents the data for two cases: a standard chop/nod method of sky cancellation, and a chop/nod method where the off-source bolometers are used to remove residual sky noise. Although the error bars are somewhat large, the standard chop/nod method seems to support the long-held belief that sensitivity decreases with chop throw (e.g. Church
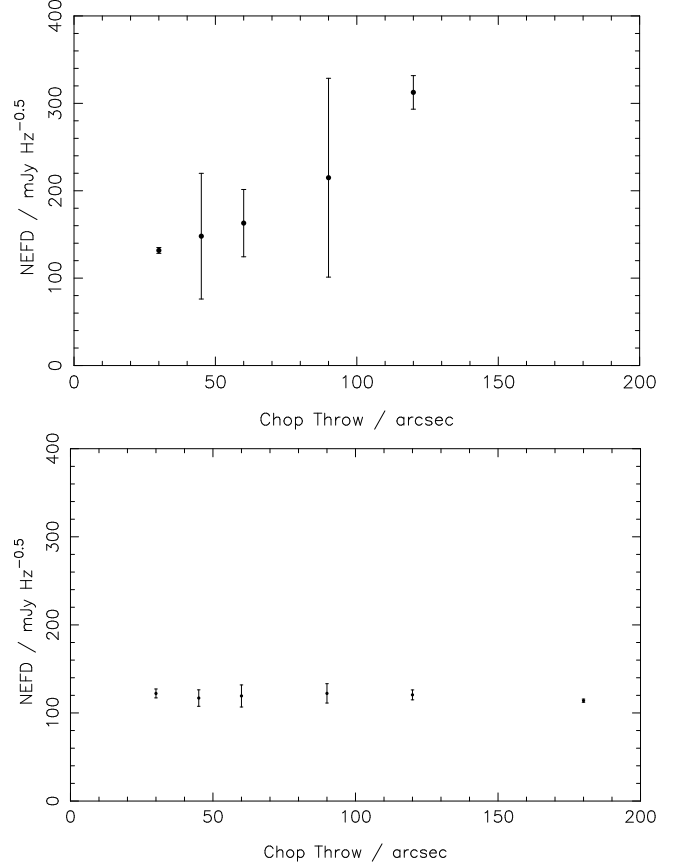
et al. 1993; Duncan et al. 1995). However, when using the array and when off-source bolometers are used for sky cancellation, large chop throws *do not* degrade the sensitivity. In this case, the NEFD vs. chop throw plot is perfectly flat out to a chop throw of 180 arcsec. The only variation is due to an increase of the FCF with chop throw, of the order of 10% between 45 and 120 arcsec (Jenness et al. 2001).

7   SUMMARY AND THE FUTURE

As described in this paper, we have a good grasp of the atmospheric limitations in the submillimetre and how best to overcome them. Our main findings can be summarized as follows:

(i) Tau relations between the CSO Tau at 225 GHz and both the 850 μm and the 450 μm SCUBA filters. The relations display relatively little scatter.

(ii) For accurate sky cancellation, it is essential to use off-source bolometers to monitor and remove the sky-noise.

(iii) There is evidence for positive correlations between sky-noise and seeing, and sky-noise and sky opacity,but the correlation coefficient varies significantly depending on the dataset Figure 11.

(iv) 850-μm and 450-μm sky-noise are clearly correlated, but there are times when the correlation is low.

(v) The JCMT beam is not significantly broadened by seeing.

(vi) There is no obvious correlation between seeing and pointing excursions.

(vii) If off-source bolometers are used for sky cancellation, chopping as far as 180 arcsec (in any direction) does not affect the sensitivity of the instrument.

In the future, as our understanding grows, as technological advances are made, and as the next generation of submillimetre telescopes are destined to higher and drier sites, we will be able to do even better. Some things to look forward to are:

(i) Line-of-sight radiometers which give real time estimates of Tau in the direction you are observing. One of these radiometers is now in operation at the JCMT (e.g. Wiedner et al. 2001, Phillips et al. in preparation).

(ii) Instantaneous estimates of the line-of-sight opacity should be possible using a hot load, cold load, and sky observation at the elevation of the source, given a database of sky temperature versus elevation information (e.g. Smith, Naylor & Feldman 2001).

(iii) High-speed data sampling leading to a more efficient observing mode called 'DREAM' (Le Poole & van Someren Greve 1998). In DREAM mode, the functions of chopping and jiggling the secondary mirror are combined to a single step action, eliminating the need to sample empty sky for half the time. Another gain from high-speed sampling is real-time suppression of sky-noise.

(iv) Adaptive optics for the submillimetre. The Large Millimetre Telescope (LMT) is currently designing a radiometric wave-front sensor which will measure the tilt of the incoming wavefront to compensate for atmosphere-induced pointing errors (For further details refer to the LMT website: http://www-lmt.phast.umass.edu/).

(v) DC-coupled fully sampled arrays such as SCUBA 2 (Holland et al. 2000; Robson et al. 2001), which would remove the necessity to chop and nod for sky-noise removal. This is an advantage: there is no chance of chopping onto a nearby source, and there will be a sensitivity gain as all the time is spent looking at the source instead of half the time looking at the sky. In addition, chopping limits the size-scales we see in maps to be no more than a few times the chop throw. Finally, image reconstruction techniques for two-beam chopping tend to propagate noise, and so with only a single-beam on the sky this problem will be minimsed.

(vi) In the future, submillimetre telescopes will be built at sites where the atmosphere is largely transparent, for example Chajnantor in Chile at 17,000 ft. (ALMA) and the South Pole. The extreme cold at the South Pole results in very small amounts of water vapour in the atmosphere, and thus sky-noise is much lower than other sites (Stark 2001).

(vii) Interferometers such as ALMA have a unique advantage: the atmospheric signals decorrelate, and therefore sky-noise should not be a problem.

REFERENCES

Allan D., 1966, Proc. IEEE, 54, 221

Borys C., Chapman S. C., Scott D., 1999, MNRAS, 308, 527

Church S., Hills R., 1990, in URSI/IAU Symposium on Radio Astronomical Seeing, pp. 75–80

Church S. E., Lasenby A. N., Hills R. E., 1993, MNRAS, 261, 705

Coulson I. M., 2001. Tech. Rep. SCD/SN/005, JCMT, (http://www.jach.hawaii.edu/JACdocs/JCMT/SCD/SN/005)

Davis G. R., Naylor D. A., Griffin M. J., Clark T. A., Holland W. S., 1997, ICARUS, 130, 387

Duncan W. D., 1983, Infrared Physics, 23, 333

Duncan W. D., Robson I., Ade P. A. R., Church S. E., 1995, in ASP Conf. Ser. 75: Multi-Feed Systems for Radio Telescopes, p. 295

Duncan W. D., Sandell G., Robson E. I., Ade P. A. R., Griffin M. J., 1990, MNRAS, 243, 126

Goldsmith P. F., 1987, International Journal of Infrared and Millimetre Waves, 8, 771

Hazell A. S., 1991, PhD thesis, Queen Mary and Westfield College

Holland W. S., Duncan W. D., Kelly B. D., Peacocke T., Robson E. I., Irwin K. D., Hilton G., Rinehart S., Ade P. A. R., Griffin M. J., 2000, in American Astronomical Society Meeting, Vol. 197, p. 5301

Holland W. S., Robson E. I., Gear W. K., Cunningham C. R., Lightfoot J. F., Jenness T., Ivison R. J., Stevens J. A., Ade P. A. R., Griffin M. J., Duncan W. D., Murphy J. A., Naylor D. A., 1999, MNRAS, 303, 659

Jenness T., Lightfoot J. F., Holland W. S., 1998, Proc. SPIE, 3357, 548

Jenness T. J., Stevens J. A., Archibald E. N., Economou F., Jessop N. E., Robson E. I., 2001, MNRAS, submitted

Le Poole R. S., van Someren Greve H. W., 1998, in Proc. SPIE Vol. 3357, p. 638-643, Advanced Technology MMW, Radio, and Terahertz Telescopes, Thomas G. Phillips; Ed., Vol. 3357, p. 638

Masson C. R., 1991, in ASP Conf. Ser. 19: IAU Colloq. 131: Radio Interferometry. Theory, Techniques, and Applications, p. 405

Naylor D. A., Clark T. A., Davis G. R., 1994, Proc. SPIE, 2198, 703

Naylor D. A., Davis G. R., Gom B. G., Clark T. A., Griffin M. J., 2000, MNRAS, 315, 622

Olmi L., 2001, A&A, 374, 348

Omont A., McMahon R. G., Cox P., Kreysa E., Bergeron J., Pajot F., Storrie-Lombardi L. J., 1996, A&A, 315, 1

Robson E. I., Holland W. S., Duncan W. D., 2001, in UMASS/INAOE Conference 'Millimetre Surveys for the Future', Lowenthal J., Hughes D. H., eds., ASP Conf. Series, in press

Schieder R., Kramer C., 2001, A&A, 373, 746

Smith G., Naylor D., Feldman P., 2001, Int. J. of Inf. and Mm. Waves, in press

Stark A. A., 2001, in Experimental Cosmology at Millimeter Wavelengths, De Petris M., Gervasi M., eds., astro-ph/0109229

Stevens J. A., Robson E. I., 1994, MNRAS, 270, L75

Tilanus R. P. J., Jenness T., Economou F., Cockayne S., 1997, in ASP Conf. Ser. 125: Astronomical Data Analysis Software and Systems VI, Vol. 6, p. 397

Wiedner M. C., Hills R. E., Carlstrom J. E., Lay O. P., 2001, ApJ, 553, 1036

APPENDIX A: SKYDIP MODEL

When performing a skydip, SCUBA measures the sky brightness temperature as a function of airmass. We present a multi-layer model of the atmosphere (Hazell 1991) which, when compared with the data, yields the zenith sky opacity. The model at each wavelength takes the form:

$$J_{meas} = (1 - \eta_{tel})\, J_{tel} + \eta_{tel}\, J_{atm} - bwf\, \eta_{tel}\, J_{atm} e^{-TauA} \quad \text{(A1)}$$

where J_{meas} is the measured brightness temperature of the sky, η_{tel} is the transmission of the telescope, J_{tel} is the brightness temperature of a black-body radiating at the temperature of the telescope, J_{atm} is the brightness temperature of the atmosphere, bwf is the bandwidth factor of the filter being used ($1 - bwf$ is the fraction of the filter bandwidth that is opaque due to atmospheric absorption and, like Tau, is a function of water vapour content), Tau is the zenith sky optical depth and A is the airmass of the measurement.

Of these parameters, J_{meas}, J_{tel} and A are known. J_{atm} can be estimated from the ambient air temperature at ground level using a model for the behaviour of the observing layer above the telescope, as described below. η_{tel} may be fitted to the data for every skydip and, because it does not vary with atmospheric conditions, a reliable 'average' value can be derived from many observations. Thus, there are two remaining free parameters, τ and bwf, that must be derived from the fit.

J_{atm} is calculated from T_{amb}, the ambient air temperature, by assuming that the sky emission is dominated by a single absorber/emitter whose density falls exponentially and temperature linearly with height. In this case it can be shown that:

$$J_{atm} = \qquad J_{amb} \int_0^{40} Ak\, exp\left(-\frac{h}{h_2}\right) \times$$
$$exp\left[Akh_2\left(exp\left(-\frac{h}{h_2}\right) - 1\right)\right]\left(1 - \frac{h}{h_1}\right)\, dh \quad \text{(A2)}$$

where h_1 is $J_{amb}/6.5$ to give a 6.5 K fall in temperature per km height, h_2 is the scale height of the absorbers (2 km), A is the airmass and k the extinction per km.

If we approximate the result of the integral by:

$$J_{atm} = J_{amb} X_g \left[1 - \exp\left(-Akh_2\right)\right] \quad \text{(A3)}$$

it can be shown that X_g has the form:

$$X_g = 1 + \frac{h_2 T_{lapse}}{T_{amb}} \exp\left(-\frac{ATau}{X_{gconst}}\right) \quad \text{(A4)}$$

where T_{lapse} is the temperature drop per kilometre altitude (-6.5 K/km) and X_{gconst} is a constant determined empirically and has a value of 3.669383.

APPENDIX B: THEORETICAL DERIVATION OF SKY-NOISE RATIO

If we consider two lines of sight separated by an angle theta and identical to each other except for the fact that one line of sight has a cloud of water vapour at a distance to which the line of sight opacity is τ_{cloud}, and the cloud itself has optical depth $\delta\tau$, then the difference in surface brightness between the two lines of sight (measured in units of brightness temperature) is simply

$$\delta J = exp(-\tau_{cloud})\, \delta\tau\, (J_{cloud} - J_{inc}) \quad \text{(B1)}$$

where J_{cloud} is the physical temperature of the cloud, and J_{inc} is the incident flux on the cloud from the upper atmosphere. In all cases it is likely that J_{cloud} is greater than J_{inc} so that the observed effect of the cloud is to increase the surface brightness along that line of sight.

If the cloud is close to the top of the water vapour column density then J_{inc} is negligible compared to J_{cloud} and one can simply write:

$$\delta J = exp(-\tau_{cloud})\, \delta\tau\, J_{cloud}. \quad \text{(B2)}$$

If one considers the signal at two wavelengths $\lambda 1$, $\lambda 2$ then the ratio is

$$\frac{\delta J_{\lambda1}}{\delta J_{\lambda2}} = \frac{exp(-\tau_{\lambda1})}{exp(-\tau_{\lambda2})}\frac{\delta\tau_{\lambda1}}{\delta\tau_{\lambda2}}, \quad \text{(B3)}$$

where we have removed the subscripts cloud. One can express this in terms of power by simply invoking the Rayleigh-Jeans law $B(\lambda) \propto J/(\lambda^2)$ so that,

$$\frac{\delta B_{\lambda1}}{\delta B_{\lambda2}} = \frac{exp(-\tau_{\lambda1})}{exp(-\tau_{\lambda2})}\frac{\delta\tau_{\lambda1}}{\delta\tau_{\lambda2}}\frac{\lambda1^2}{\lambda2^2}, \quad \text{(B4)}$$

and also to measured volts by applying an appropriate FCF

$$\frac{\delta V_{\lambda1}}{\delta V_{\lambda2}} = \frac{exp(-\tau_{\lambda1})}{exp(-\tau_{\lambda2})}\frac{\delta\tau_{\lambda1}}{\delta\tau_{\lambda2}}\frac{\lambda1^2}{\lambda2^2}\frac{FCF_{\lambda2}}{FCF_{\lambda1}}. \quad \text{(B5)}$$

In the case where the opacities are simply proportional to water vapour column density (as we have shown in this paper) then $\delta\tau_{\lambda1}/\delta\tau_{\lambda2}$ is a constant, and we expect the ratios of the signal at the two wavelengths to be proportional to the ratios of transmission from the cloud to the telescope at the two wavelengths. One also expects

$$\frac{\delta J_{\lambda1}}{exp(-\tau_{\lambda1})} \propto \frac{\delta J_{\lambda2}}{exp(-\tau_{\lambda2})} \quad \text{(B6)}$$

where one has to be careful to note that the value of τ is to the cloud, not all the way to the top of the atmosphere.

For the SCUBA filters the ratios of $\delta\tau_{850n}/\delta\tau_{450n}$ and $\delta\tau_{850w}/\delta\tau_{450w}$ have been measured earlier in this paper. Jenness et al. (2001) have measured the FCFs from point sources using a 60 arcsecond radius aperture, which are also (by symmetry) valid for a uniform extended source of size 60 arcseconds. In the section on sky noise in this paper most of the photometry observations were taken with 60 arcsecond chop throws so that the skynoise measured is a measure of the difference in signal between two largely (but not exactly) overlapping regions of diameter 15 meters, 60 arcseconds apart. If the cloud is at a height, h above the telescope then the diameter of the beam in steradians is 15/h(m) or 25 arcminutes at a height of 2 km. This explains why the sky noise is uniform over the array.

In Fourier space we can consider the beam as a high spatial frequency filter of the form

$$exp\left(\frac{-k^2}{15}\right) \tag{B7}$$

i.e. one that filters out spatial scales $< 15\,\mathrm{m}$ and the chop as a low spatial frequency filter of the form

$$sin(2\,\pi\,k\,c\,h) \tag{B8}$$

where k is the wavenumber, c is the chop throw in steradians, and h is the height of the cloud in metres. This can be simplified to $2\pi kch$ for the frequencies that are passed by the beam. The effect of having two differing spatial frequency filters is to couple only weakly (at a level $ch/15$) to clouds of approximate spatial scale $15\,\mathrm{m}$. Clouds smaller than this are filtered out by the beam, clouds larger than this are filtered out by the chop throw. For typical values ($h = 2\,\mathrm{km}$, $c = 60\,\mathrm{arcseconds}$), the coupling is only 4 percent - illustrating how effective chopping is as a first stage to removing sky noise.

Although strictly speaking the FCFs calculated by Jenness et al. (2001) are only valid for extended far field objects, one can use the ratio of the values measured as an estimate of the ratio of the FCFs which would be valid for nearfield extended objects (i.e. the cloud in question). The validity of this assumption can then be assessed by comparison with the data.

If one therefore uses the various values discussed in the previous paragraph then one finds:

$$\frac{\delta V_{450W}}{\delta V_{850W}} = 6.64\,\frac{exp(-\tau_{450W})}{exp(-\tau_{850W})}, \tag{B9}$$

$$\frac{\delta V_{450N}}{\delta V_{850N}} = 3.32\,\frac{exp(-\tau_{450N})}{exp(-\tau_{850N})} \tag{B10}$$

and

$$\frac{\delta B_{450W}}{\delta B_{850W}} = 23.2\,\frac{exp(-\tau_{450W})}{exp(-\tau_{850W})}, \tag{B11}$$

$$\frac{\delta B_{450N}}{\delta B_{850N}} = 21.2\,\frac{exp(-\tau_{450N})}{exp(-\tau_{850N})} \tag{B12}$$

Given that we have shown we are coupling to sources larger in scale than 60 arcseconds, we could further correct these values by the ratio

$$\frac{\eta_{450(cloud)}}{\eta_{850(cloud)}}\,\frac{\eta_{850(60")}}{\eta_{450(60")}} \tag{B13}$$

where η is the coupling. However, given uncertainties in the cloud's angular size (principally due to uncertainties in its height), and the fact that the ratio of the coupling values is likely to vary less significantly than the individual values, we choose not to.

APPENDIX C: REFRACTION

C1 Refraction Code at JCMT

The primary purpose of the current JCMT refraction model is to provide coarse corrections to pointing based on local atmospheric conditions. It assumes a well-behaved, non-turbulent atmosphere. To first order, refraction displaces images towards the zenith by an amount

$$R = A * tan(z) \tag{C1}$$

where z is the zenith distance, and A is a function of the local atmospheric parameters :

(i) T - Temperature (above some mean, chosen as 4 K for Mauna Kea)

(ii) p - % Pressure change from the MK standard of 624 mb
(iii) h - % Humidity

Grids of atmospheric models were generated and refraction calculated at several zenith distances by integrating through the atmosphere. Simple functional forms of the results were sought that would enable calculation of refraction from local atmospheric conditions. The optical- and millimetre- A-terms in the formula above take principally these forms (units are arcseconds) :

$$A = 35.893 - 0.00067(h - 20) - 0.135(T - 4) + 0.371p \tag{C2}$$

at $0.55\,\mu\mathrm{m}$ and:

$$A = 36.800 + 0.0768(h - 20) - 0.0294(T - 4) + 0.371p \tag{C3}$$

at 1 mm.
- i.e. optical refraction is dependent mostly upon temperature, while submillimetre refraction is dependent mostly upon humidity. The 1 mm formulation used at JCMT contains additional, less significant terms. Its values were compared to the integration results throughout the grid and were found to be accurate to better than 1 arcsec for zenith distances less than 80 degrees under all but the most extreme conditions.

C2 Expectation Values of Signal Levels in the Presence of Refraction

This appendix describes the use of the pointing rms values determined from the SAO phase monitor to give an indication of the expectation values of the signal levels, relative to the values for no refraction 'noise'. The assumptions are

(i) the refraction noise can be described by a Gaussian process, which in two dimensions gives the Rayleigh distribution:

$$P_\theta = \frac{\theta}{\sigma^2}\,exp\left(\frac{-\theta^2}{2\sigma^2}\right) \tag{C4}$$

where P_θ is the probability of the refraction having a value of θ arcsecs, and σ is the rms refraction 'noise'.

(ii) the telescope beam can also be defined as a Gaussian:

$$S(\theta) = S_o\,exp\left[-4ln(2)\frac{\theta^2}{\theta_{fwhm}^2}\right] \tag{C5}$$

where S is the signal level which would be measured for a movement of the telescope of θ arcsecs, and θ_{fwhm} is the FWHM size of the beam in arcsecs.

The expectation value of the signal level, relative to the no refraction noise case, is given by

$$< S > = \frac{\int_0^{S_o} S\,P_S\,dS}{\int_0^{S_o} P_S\,dS} \tag{C6}$$

where P_S is the probability distribution for the signal.
Probabilities transform directly so that

$$P_S\,dS = P_\theta(-d\theta) \tag{C7}$$

where use is made of the fact that the probability of S decreasing is a function of the probability of θ increasing.
For simplicity, we rewrite (C5) as

$$S(\theta) = S_o exp\left[-\frac{\theta^2}{2\beta^2}\right] \tag{C8}$$

where $\beta^2 = \frac{\theta_{fwhm}^2}{8ln2}$.

Now, from equation (C8),

$$\frac{dS}{d\theta} = -\frac{\theta}{\beta^2}S \qquad (C9)$$

using this and equations (C4),(C8),

$$P_S = \frac{\beta^2}{\sigma^2}\frac{1}{S}\left[\frac{S}{S_o}\right]^{\frac{\beta^2}{\sigma^2}} \qquad (C10)$$

It should be noted that, if $\beta^2 = \sigma^2$, the probability is uniform.

If we now evaluate (C6) using (C10) we find that

$$\frac{<S>}{S_o} = \frac{1}{1+\frac{\sigma^2}{\beta^2}} = \frac{1}{1+\frac{8ln2\sigma^2}{\theta_{fwhm}^2}} \qquad (C11)$$

In the case of a perfect 15-metre telescope, one can write for θ_{fwhm} in arcsecs :

$$\theta_{fwhm} = [14.025 + 0.1856T_E]\lambda \qquad (C12)$$

where T_E is the illumination edge taper in decibels and λ is the wavelength in mm (Goldsmith 1987). The edge taper determines the level of ground radiation accepted by the feed, and at JCMT $T_E \sim 7.5\,\text{dB}$. In the case of a telescope with surface imperfections one must use the measured value of the full width half-maximum beam size in (C11).

If we assume a $14.2''$ beam at $850\,\mu\text{m}$ and a $7''$ beam at $450\,\mu\text{m}$, then (C11) becomes

$$\frac{1}{1 + 0.0275\sigma^2} \text{ for the 14.2" beam} \qquad (C13)$$

and

$$\frac{1}{1 + 0.1132\sigma^2} \text{ for the 7" beam} \qquad (C14)$$

where σ is the rms refraction noise in arcseconds.